JOURNAL OF THERMOPHYSICS AND HEAT TRANSFER
Vol. 24, No. 4, October–December 2010

Thermal Protection System Crack Growth Simulation Using Advanced Grid Morphing Techniques

E. V. Titov* and D. A. Levin†
Pennsylvania State University, University Park, Pennsylvania 16802
Donald J. Picetti
The Boeing Company, Huntington Beach, California 92647
and
Brian P. Anderson
NASA Johnson Space Center, Houston, TX 77058

DOI: 10.2514/1.48046

An extension of previous [Titov, E., Zhong, J., Levin, D., and Picetti, D., "Simulation of RCC Crack Growth Due to Carbon Oxidation in High-Temperature Gas Environments," *Journal of Thermophysics and Heat Transfer*, Vol. 23, No. 3, July–Sept. 2009, pp. 489–501.] modeling of crack damage growth in reinforced carbon–carbon specimens is presented in this work. The specimens were studied in an arcjet and represented a portion of the space shuttle wing [Lewis, R., "Quick Look Report," *Atmospheric Reentry Materials and Structures*, 2004.] and a high-velocity meteoroid impact [Curry, D. M., Pham, V. T., Norman, I., and Chao, D. C., "Oxidation of Reinforced Carbon–Carbon Subjected to Hypervelocity Impact," NASA TP 2000-209760, March 2000.]. The test geometry and flow conditions rendered the flow regime as transitional to continuum; therefore, a Navier–Stokes-based gas-dynamic approach with the temperature jump and velocity slip correction to the boundary conditions was used. The modeled mechanism for wall material loss was atomic oxygen reaction with the bare, exposed carbon surface. The purpose of this work is to improve the predictive modeling of crack growth damage assessment by developing procedures that use coupled, advanced topology-based surface and grid-meshing tools. A recessing three-dimensional surface morphing procedure was developed and tested by comparison with arcjet experimental results. A multiblock structured adaptive meshing was used to model the computational domain changes due to the wall recession. This approach made it possible to model full three-dimensional crack growth scenarios as well as to include the presence of realistic reinforced carbon–carbon material features such as delamination, both of which affect damage growth because they enable higher atomic oxygen penetration. Comparison with the arcjet data show that the inclusion of these two factors further improves the comparison between modeling and data. The predicted channel growth and shape change were found to agree with arcjet observations, and local gas flowfield results were found to affect the oxidation rate in a manner that cannot be predicted by previous mass loss correlations. The method holds promise for future modeling of materials gas-dynamic interactions for hypersonic flight.

I. Introduction

THE reinforced carbon–carbon (RCC) nose cap and wing leading edge of the space shuttle are vulnerable to cracks that can be formed through micrometeoroid and orbital debris (MMOD) impact [1]. During Earth atmospheric reentry, the freestream species, especially reactive atomic O, can penetrate through the exposed carbon-crack material and cause damage site expansion through atomic oxygen reactions. The resulting growth of the damage site can pose severe structural damage to the wing and the nose portion of the vehicle. To develop a simulation tool that can predict the degree of crack growth during reentry following a MMOD impact, a physical model must be proposed and an iterative material response gas-dynamic flow computational approach must be developed. The main emphasis of this paper is to discuss the second aspect, since, a physical model of crack growth due to atomic oxygen was discussed in our previous work [2]. The operational considerations of RCC/shuttle oxidation and conditions of reentry have been considered by a number of authors [1,3–5]. Reinforced carbon–carbon thermal protection material is composed of graphite fibers embedded in a carbon matrix. The composites are coated with a layer of silicon carbide (SiC), which has the role of protecting the bare composite from oxidation [6–10]. Unlike other studies that have been concerned with understanding the robustness of the silica layer, our starting conditions are based on the concept that a known region of the protective SiC layer has been removed and that only bare carbon is exposed. The portions of the sample for which this occurs are given by the arcjet sample specifications, as will be discussed further in Sec. II.

In our previous effort we proposed a wall oxidation model relevant to the conditions in the NASA Johnson Space Center arcjet tests of [11]:

$$C_{(s)} + O \rightarrow CO \tag{1}$$

where, the temperature of gaseous atomic O is about 1500 K, $C_{(s)}$ is a carbon atom at the wall surface, and the other species are gaseous. The measurements of Rosner and Allendorf [12,13] show that for atomic oxygen collisions with a carbon surface atom, the probability of carbon atom removal is close to unity over a surface temperature range of 1000 to 1600 K for a fairly low activation energy of 6.8 Kcal/mole. A probability for the reaction, based on [13], of 0.9 was used in all simulations. (Note that the probability of removal for molecular oxygen is about a factor of 50 lower.) Using this single reaction for three arcjet cases varying from near continuum to continuum conditions, based on a Knudsen number defined by the crack dimension, we were able to obtain good agreement between

Presented as Paper 2009-3599 at the 41st AIAA Thermophysics Conference, San Antonio, TX, 22–25 June 2009; received 8 November 2009; revision received 18 April 2010; accepted for publication 23 April 2010.

*Postdoctoral Scholar, Department of Aerospace Engineering. Member AIAA.
†Professor, Department of Aerospace Engineering. Associate Fellow AIAA.

our simulations and the arcjet data in terms of damage shape change and degree of mass loss. The research showed that local gas flowfield features were found to affect the oxidation rate in a manner that cannot be predicted by previous mass loss correlations [14], particularly for crack geometries that are highly three-dimensional in nature.

However, the work left open the two important issues. For complex three-dimensional geometries, it was found that it was not possible to allow the surface to regress in a true three-dimensional manner because the time evolution of the surface could not be automated and was too complex to change manually. Instead the wall geometry of the machined channel crack was modeled using a linearized three-dimensional approximation of the side walls of the channel. This approximation provided a worst case estimate of the wall destruction and the crack growth, and, qualitatively showed the correct shape change. Moreover, the simulations were only able to model the channel growth for conditions corresponding to 50 s, whereas, the actual arcjet exposure lasted about 420 s. The second issue was that even for an axisymmetric hypervelocity impact case, our work did not consider the important RCC material property of delamination. MMOD damage samples of RCC materials show that macroscopic material delaminations look like small microchannel regions which can create local stagnation regions in the damage site area. The local flow properties in the microchannels and in particular at their entrances can contribute to the material degradation process causing the relatively large chunks of material to break away when the chemistry at the walls of the microchannels weakens the structural strength of the material [15]. As will be shown in this work, the introduction of such RCC materials properties introduces yet another length scale to the flow over the body or specimen and the flow through the crack requiring a true multiscale solution.

Both the two-dimensional approximation and the lack of delamination structure approximations affect the modeling quality of the wall destruction process, atomic oxygen penetration. The purpose of this work is to remove these two aforementioned constraints by using advanced topology-based surface and grid-meshing tools that will couple the surface changes with the computational fluid dynamics (CFD) volume meshing. To the best of our knowledge, this is the first application of topology-based meshing to a flow-material multiscale problem with morphing boundaries. For local gas-dynamic features to be resolved, adequate meshing of the dynamically changing computational domains must be addressed. This in turn requires a comprehensive multiscale meshing technique to be applied since fractures, channels, or holes created by hypervelocity impacts and other surface imperfections can introduce important small-scale geometric details that must be resolved by the analysis grid. In many cases, the resulting effect on the local gas dynamics must be coupled with the remainder of the vehicle flowfield. In addition, surface degradation of the thermal protection system (TPS) material causes the vehicle geometry to change in time, and with holes or fractures, the surface degradation can be highly irregular. Flow analyses in the presence of such conditions requires automated adaptive techniques in order to regenerate the surface and volume grids as a function of time.

For the class of TPS materials of current interest, several assumptions can be made. First, the time scale of the surface degradation is longer than the time scale for formation of the surrounding flowfield. Therefore regression rates appropriate for a given type of TPS material can be calculated at each instant from the steady-state flowfield solution. Secondly, the physical mechanisms that cause the surface regression can be specified although they are specific to the particular TPS material and flight environment. For the shuttle-RCC system, the surface regression rate is dominated by atomic oxygen chemical attack of exposed bare carbon [Eq. (1)]. Once the surface regression has been calculated, the surface geometry must be modified, the surface mesh must be updated, and finally, the flow or finite-volume mesh must be reconstructed. This process must be repeated several times to obtain the crack or hole growth damage rate and spatial evolution, which mandates that the process must be automated to the extent possible. The surface geometry is modified according to the regression rates along surface normals. However, since the fracture geometry can be very irregular, containing corners, ridges, and other highly convex and concave regions, care is needed in converting the regression distances into a new surface representation.

To develop the automated procedure outlined above, one must select either a structured or unstructured meshing approach for the computational flow domain. It is generally preferable to use structured meshes in cases with predictable flow features because the user can anticipate these local flow features, such as boundary layers and shock waves, to direct the meshing software accordingly. Structured meshes are also known to produce high-quality flow solutions at a faster convergence rate. The stability of the flow solution algorithm on the structured mesh is also higher than on the unstructured mesh [16].

The preprocessing for the structured mesh is, however, more involved than for an unstructured mesh. The generation of the structured mesh is further challenged by the need to resolve local flow features in the microchannel damage site areas along with the overall flow upstream of the channel and crack entrances. In this work we successfully used structured meshing of the microchannel and the external flow by creating a single mesh that covers the entire computational domain and was capable of adapting to the changing shape of the recessing surfaces. To achieve this, we employed multizone topology-based meshing where boundaries of each of the zone are allowed to change, making, a more uniform distribution of cell sizes while resolving the flow features. Two principles are used to make such a procedure possible. The first one is the adoption of a topology-based representation of the computational domain [17] and the second is the mesh node equidistribution principle [18,19]. Both principles are the key ingredients of the GridPro [19] software which we made use of in this research.

The topology-based domain representation is a powerful technique which allows the effective meshing of computational domains with evolving boundaries, if the topology of such domains does not change. We will discuss these principles further in Sec. III. Topology-based meshing was studied in [17] where a representation for a mesh based on the topological hierarchy of vertices, edges, faces and regions, is described. The authors consider a mesh as a database of such elements capable of answering complex queries posed by the applications. In their approach the informational requirements for a general purpose mesh database for automated adaptive finite element analysis on domains defined by manifold geometric models are first defined. Then a mesh database based on a topological hierarchy designed to meet these requirements is created. The authors studied the storage overhead required to support the database topology information and conclude that it is small compared with the mesh storage itself.

The topology-based modeling of three-dimensional surfaces, which is crucial for our repeated meshing of the carbon recessing surface, was studied in [20–22]. The authors proposed and implemented a conceptional framework which guarantees topologically correct two-dimensional manifolds and provides a new user interface paradigm for mesh modeling systems. Before this work, despite significant effort in topology-based surface meshing, a general method which guaranteed surface meshes free of spikes, collapses or other mesh imperfections was not available. They proposed an alternative Morse operations-based technique and provide evidence of its superiority over the traditional set operations-based methods.

The second principle, equidistribution, is a fundamental principle in mesh generation which is the generation of a grid with mesh points evenly distributed along a curve (one-dimensional), a surface (two-dimensional) or a volume (three-dimensional) [23]. Many approaches exist to perform the equidistribution including Green's function techniques [24], weight functions [25], and variational approaches such as presented in [26,27]. The mesh adaptation approach presented in [19] rests on the principle of equal amounts of a specified weight function. When the generation process is performed, the gradients of the monitor surface are used by the weight function along with other quantities such as background node density to distribute or cluster the mesh points according to, for example, the flow gradients. The mesh adaptation approach of [19]

will be used in the cases studied in this work, as will be illustrated in Secs. IV and V.

The remaining portions of the article will discuss the surface regression model developed in this research along with topology-based meshing applied to the microchannel growth problem. The numerical results obtained for two damage site configurations will be compared with the results of arcjet tests as is discussed in the next section. In Sec. III we discuss the methodology that we developed for the volume and surface meshing for RCC morphing geometries. We then demonstrate the procedure and compare the simulated results with arcjet measurements for the 1151 hypervelocity impact case in Sec. IV and for the 2033 case in Sec. V. We will show that the procedure is capable of predicting the arcjet data in a manner that has not been possible before. This procedure has been transferred to personnel at the NASA Johnson Space Center and is being further organized to support near-real time on-orbit shuttle damage assessment.

II. Experiment Conditions

A high-energy flow is generated in the arcjet facility through an expansion of the heated and pressurized gas through a supersonic nozzle. Figure 1 presents the two samples that are studied in this work, Cases 1151 and 2033. The left and right hand sides of the figure show the samples before and after exposure to the arcjet flow. It is clearly visible from the figure that the initial stagnation point hole, for Case 1151, and the initial microchannel for Case 2033 significantly expand, when subjected to the arcjet flow conditions similar to that during the vehicle Earth atmosphere reentry. The schematic of the sample holder in the arcjet is shown in Fig. 3 of [2]. The non-equilibrium arc-tunnel analysis (NATA) code provided the freestream conditions representative of the upstream arcjet shock conditions and conditions for both cases are presented in Table 1. A Navier–Stokes (N–S) solution to a similar case is reported in [28] and good agreement with the NATA results was observed. For the calculation presented in this paper the wall temperature was kept constant at 1831 K. For the hypervelocity impact cases, of which Case 1151 is one set of measurements, the diameters of the forward and aft facing portion of the hole were measured as a function of time [1]. For the 2033 case [29], only the channel shape was recorded before and after an exposure time of approximately 420 s.

Table 1 NATA predicted free-arcjet freestream conditions[a]

	RCC Case 1151	RCC Case 2033
N_2	0.182	0.177
O_2	3.355e − 6	0.033
N	0.568	0.551
O	0.250	0.239
NO	2.49e − 6	2.426e − 6
Temperature, K	900	929
Pressure, Pa	141.6	151.07
Mach number	5.83	5.77
Wall temperature	1831	1831

[a]Freestream conditions taken from a separate arcjet CFD calculation upstream of the arcjet shock.

III. Computational Domain and Recessing Surface Morphing

A. Topology-Based Meshing

In general, block structured meshing is a well defined notion, i.e., the computational domain is divided into blocks and each of the blocks has a structured mesh. On the other hand, topology is a more abstract notion related to the geometric organization of space. For example, one can think of geometrical figures as topology elements, but not all geometrical figures represent distinct topology types. The concept behind the Gridpro [19] meshing tool rests on the idea that the topology remains unchanged even though the shape of the corresponding geometrical entities (blocks of mesh in this case) changes to some extent.

To mesh the volume regions, one must cover them with wireframe topologies that approximately follow their surface boundaries. The wireframe consists of topology nodes and edges and an assignment process is required to define to which particular boundary one or another piece of topology belongs to. The Gridpro software [19] can work with loosely positioned topologies, i.e., it can grid a topology which is defined with nodes and edge positions that only roughly conform to the desired (corresponding) geometry. If a topology element (a node or an edge) is positioned too far from a surface, it will not create a fatal error, but, the meshing process will take longer than it otherwise should. There is no a priori way to tell how close the topology elements should be placed with respect to the corresponding surfaces. The trade off is that the closer a topology resembles the actual geometry, the faster the meshing procedure will converge. The final mesh quality does not depend on how close the topology elements are located to the corresponding surfaces, but, errors in the topology itself, or a topology which does not properly reflect the underlying computational domain, may result in a fatal problem during the meshing procedure or a mesh of poor quality.

Gridpro [19] grids flow volumes in both two and three dimensions and therefore topologies can be two and three-dimensional in Gridpro. The 1151 case is solved in two dimensions while 2033 is a full three-dimensional case. In two dimensions, gridded blocks are represented by convex quadrilaterals, or quads and in three dimensions, gridded blocks are represented by convex hexahedrons.

As an example of the interaction of topology and volume meshing we consider the 1151 case. Before volume meshing, the computational domain is decomposed into topology quads. As mentioned above, different topologies will produce meshes of different quality. Figure 2a presents the simplest possible topology consisting of 18 topology elements and 14 topology nodes. As can be seen, the topology presented in Fig. 2a roughly mimics the domain boundaries and physical surfaces presented in Fig. 2b, however, two observations can be made. The first one is that the computational domain

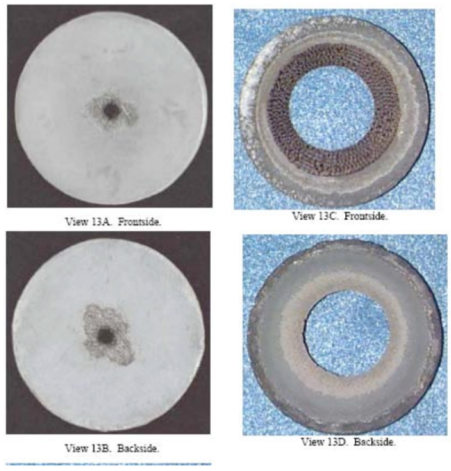

a) Case 1151

b) Case 2033

Fig. 1 Summary of two arcjet cases studied in this work.

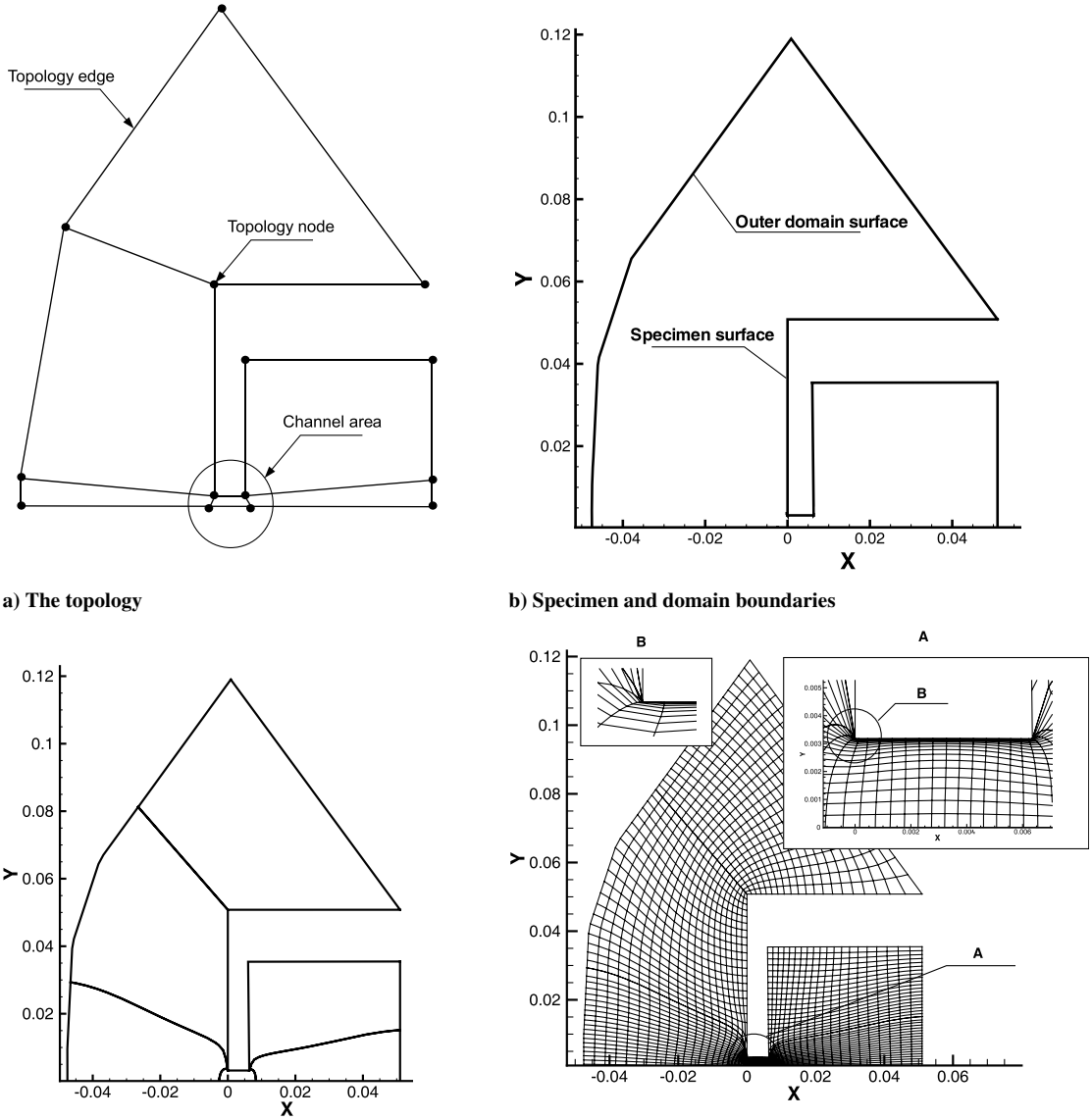

a) The topology

b) Specimen and domain boundaries

c) Mesh block structure
Lines indicate the morphed topology edges

d) The resulting mesh

Fig. 2 1151 simplified topology meshing approach.

represented by the two-dimensional surfaces in Fig. 2b exactly describes the specimen and the outer domain boundaries while the topology presented in Fig. 2a has a similar shape but its edges and nodes do not necessarily lay on the surfaces. The second observation is that even this simple topology contains some additional edges and nodes which are not required to define the domain boundaries and body surfaces. These required topology edges and nodes are created anticipating the structure of the mesh blocks, rather than the geometry of the case. The topology nodes are assigned to the corresponding surfaces, which in this case is rather obvious and one proceeds with the meshing. Figure 2c presents the resulting mesh-block structure obtained after a few hundred steps of the meshing procedure solving the variational equations as defined by the underlying algorithm [19]. As can be seen in the figure the resulting block structure is topologically equivalent to the wireframe structure presented in Fig. 2a, however, the outer boundaries of the mesh blocks now exactly match the boundaries of the 1151 specimen and the computational domain. The inner boundaries of the mesh blocks have also been modified to create an optimum mesh structure based on the provided topology.

With respect to the mesh itself, it is kept relatively coarse for this illustrative example to reduce clutter. Figure 2d presents the entire mesh for the case 1151 with an enlargement of the channel area presented zoomed in the insertion *A* and the corner of the channel entrance shown in insertion *B*. As can be seen in Fig. 2d, the overall mesh quality is reasonably good with acceptable meshing inside the channel. However, it can be seen in insertion *B* that the mesh at the corner of the channel entrance is actually of a poor quality. None of the quality criteria such as orthogonality or skewness can be satisfied with such a mesh. In fact if one attempts to use such a mesh to obtain a CFD solution, the solver will probably fail or produce some unphysical results, at best.

To improve the mesh quality, we have to understand what causes the singularity at the corner of the channel. In this case, the singularity arises because four topology edges converge at the corners of the channel, but only two surface edges are present. To avoid this we define a new 1151 topology as shown in Fig. 3a. Figure 3b presents the new surfaces defining the computational domain. There are several differences between the previous and the new topology and corresponding surfaces used in the domain modeling. The first difference is the addition of the so called artificial surfaces which can be observed in Fig. 3b. These surfaces do not represent real boundaries of the computational domain and their sole purpose is to resolve the singularity issue at the corners of the specimen. Their presence, however, must be reflected in the topology structure for the effect to take place. As can be seen in Fig. 3a several new topology

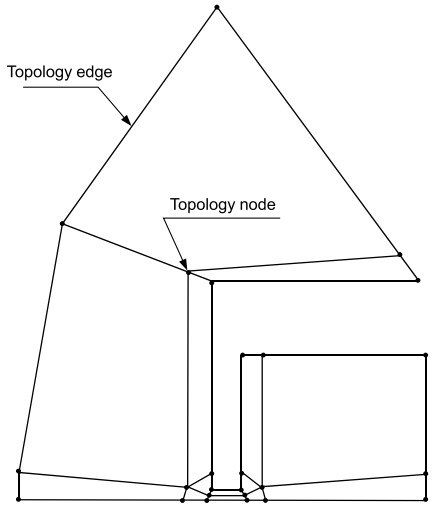

a) This is still a 2-D topology with all of the new topology nodes lying in the same plane with the original topology nodes

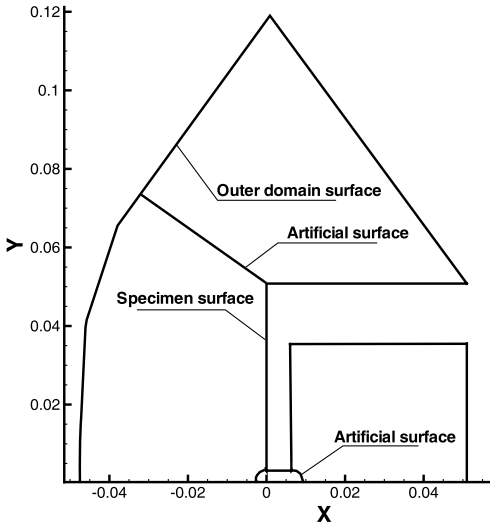

b) 1151 domain representation with artificial surfaces

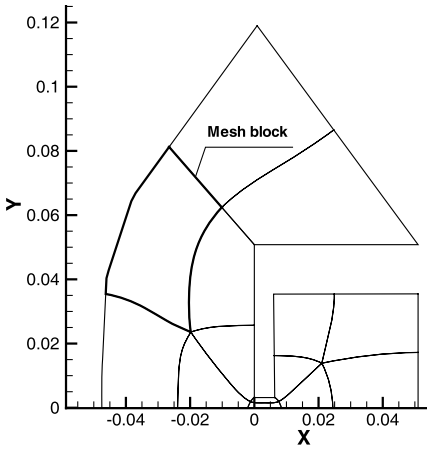

c) Mesh block structure

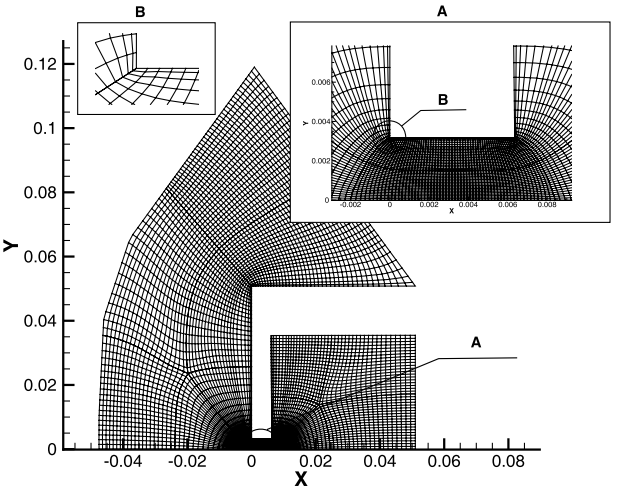

d) The improved mesh

Fig. 3 1151 improved topology meshing approach.

blocks have been added corresponding to the new domain model, causing topology nodes to be partly reassigned to the new surfaces. Some of the nodes will now have double or triple assignments, e.g., the topology node located at the corner of the channel entrance is now assigned to the three surfaces: the channel wall, the specimen outer surface, and to the artificial surface located at the entrance of the channel.

The block structure of the new 1151 mesh created by the new topology is presented in Fig. 3c. It is immediately clear from the observation of the block structure that the meshing problem at the corner of the channel entrance is now corrected. The angles at the corners of the blocks are close to 90 deg, which is a good indication of the mesh orthogonality in the past problematic areas. The boundaries of the blocks are also adapted to produce a better mesh based on the new version of the topology. Figure 3d presents the entire mesh for the domain with an enlargement of the channel area presented in the insertion *A* and the corner of the channel entrance presented in the insertion *B*. As can be seen in the figures, and, in particular in the insertion *B*, the mesh quality is improved dramatically.

To quantify the improvement we apply the mesh quality check methodology described in [30]. We measure two major mesh quality parameters for the created meshes. The first one is the local mesh orthogonality θ_k defined as intersection angle of the grid lines according to the following formula:

$$\theta_k = \frac{2}{\pi}\cos^{-1}\left(\frac{\mathbf{r}_i \cdot \mathbf{r}_j}{|\mathbf{r}_i||\mathbf{r}_j|}\right)$$

The θ_k value ranges from a minimum of 0 for a collapsed cell to a maximum of 1 for an orthogonal intersection. The second parameter is the stretching ratios $\varepsilon_i, \varepsilon_j$ computed by dividing the largest cell size by the smallest cell size on either side of a given grid point as follows:

$$\varepsilon_i = \frac{\max(|\mathbf{r}_i|^+, |\mathbf{r}_i|^-)}{\min(|\mathbf{r}_i|^+, |\mathbf{r}_i|^-)} \qquad \varepsilon_j = \frac{\max(|\mathbf{r}_j|^+, |\mathbf{r}_j|^-)}{\min(|\mathbf{r}_j|^+, |\mathbf{r}_j|^-)}$$

where: $\mathbf{r}_i$ and $\mathbf{r}_j$ are the sizes of the cell sides in i and j directions.

Figure 4 presents a comparison of the mesh orthogonality, and Fig. 5 presents mesh i and j stretch ratios for two meshes, the initial mesh, presented earlier in Fig. 2 and the improved mesh presented in Fig. 3. Note that Figs. 4 and 5 present the mesh quality in the channel area where the worst values were found. The other areas of the mesh are of good quality for both of the meshes with the average mesh orthogonality of 0.8 and 0.9 for the simple and for the improved meshes, respectively. As can be seen in the figures the mesh quality has significantly improved at the corners of the channel when the advanced topology was used and this improved mesh can easily be used in the CFD computations. One additional implication of using

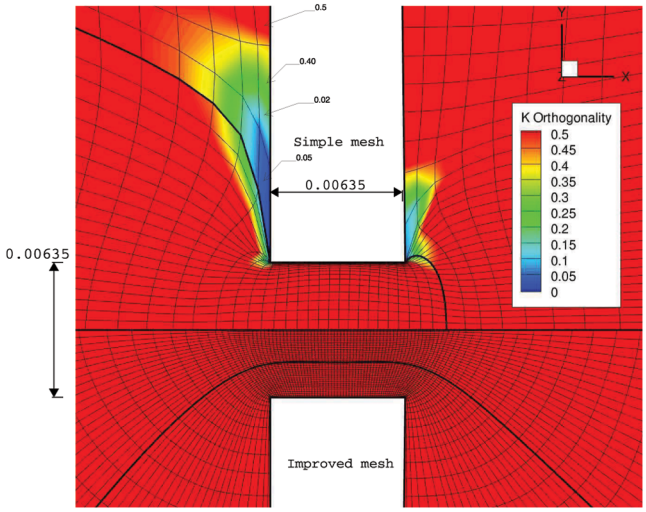

Fig. 4 Comparison of the mesh quality in terms of mesh orthogonality for the simple and improved meshes. Note that the highest contour level represents orthogonality values of 0.5 and higher.

the artificial surfaces is the improved ability to manipulate the local mesh density. In the 1151 case we want the mesh to be dense inside the channel to resolve the area of interest and less so in the outer portion of the domain. With the artificial surfaces in place, such a computationally efficient mesh can be produced. The artificial surfaces bound the interior of the channel preventing the mesh optimizer from moving the mesh points located inside the channel into the areas in front and behind the channel.

B. Three-Dimensional Surface Expansion Modeling

To model the regressing walls of highly irregular shapes a general surface morphing procedure which accounts for the local wall oxidation was developed. The procedure described here rests on the assumption that initial surface is smooth (no sharp corners) and is defined as a set of adjacent quads. To define a surface mesh element we have to specify the surface node coordinates as well as the connections between the nodes. The surface normals are defined by taking cross products of two arbitrary edges of the surface mesh quads sharing the same node. Such a procedure, in general, does not guarantee the uniqueness of the surface normal direction at each of the locations with respect to a particular surface side. To uniquely define the directions of the surface normals we make use of an external point whose position with respect to the surface sides is known. A vector connecting the external point back to the surface forms one angle with respect to an externally pointing normal and the supplementary angle with respect to an internally pointing normal. If the internal pointing vector has the larger angle, then the direction of the normal is reversed. The normals are associated and stored with each of the surface element. If nodes are shared among several surface elements (which is usually the case), an averaging is done to compute the normals associated with the surface nodes and the resulting normal direction is a sum of the normalized vectors defining these normals. We provide reference points whose coordinates are given with respect to the origin of the computational domain so that in an absolute sense the inside and outside of the channel is known. Based on these reference points, the directions of the normal vectors associated with each of the surface nodes are adjusted to be uniformly directed with respect to the surface side. The degree of surface morphing is so high that without an external reference point, the normals of two adjacent surface elements can easily point in opposite directions. We start with a control net-based channel surface created in Gridpro. We mesh the computational domain using the channel surface as one of the boundaries and run the Gasp [31] N–S solver to obtain a CFD solution. A stand alone morphing code reads the initial channel surface mesh data and the CFD solution results and then computes the normal surface vectors as the cross products of the surface element edges.

The next step is to find a closest volume node for each surface node with the values of the computational results to be associated with the surface nodes. The local oxidation rate at each surface node is computed then and stored. With the local oxidation rate and the normal direction obtained, each of the surface elements is accordingly moved. The movement of the nodes is done in a time loop incremented with the time steps that are much smaller than the time between sequential CFD runs. Visual surface mesh quality control is achieved by taking the morphed mesh back into Gridpro and checking that the resulting surface is sufficiently smooth.

If there are imperfections due to the collapse of surface elements, the procedure is restarted and run up to the time where the surface mesh was still smooth. This intermediate surface mesh serves as a reference for an analytical approximation. After trial and error, it was found that a parabolic approximation to the channel surface was

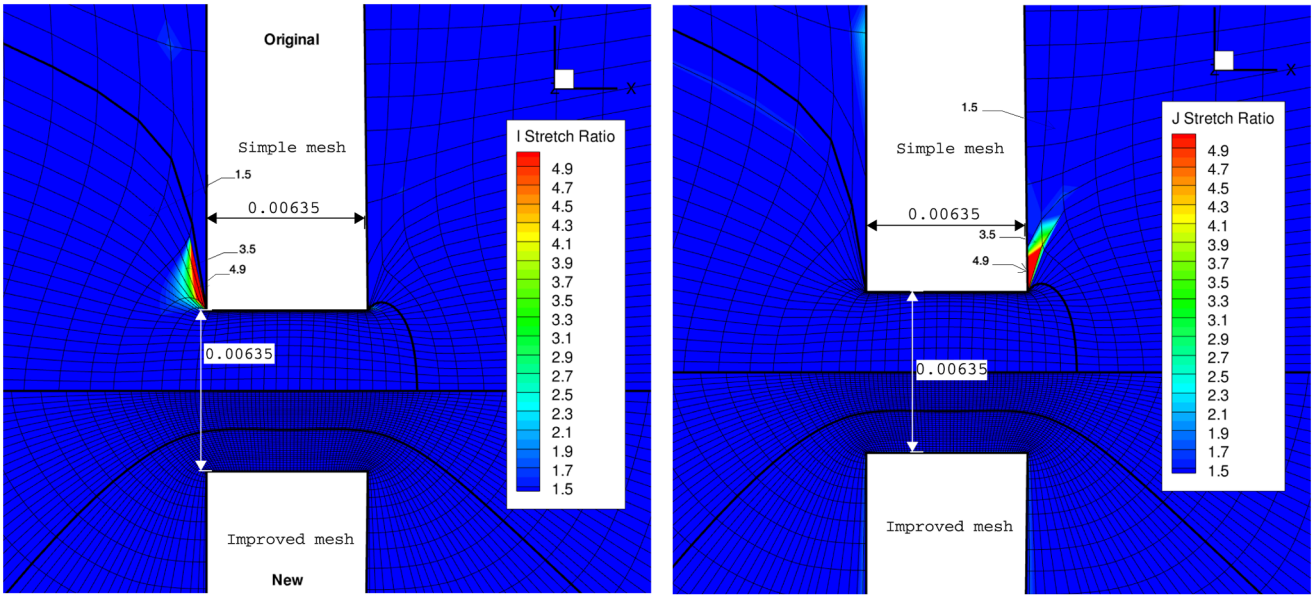

a) i-stretch **b) j-stretch**

Fig. 5 Comparison of the mesh quality in terms of mesh stretch for the simple and improved meshes. Note that the lowest contour level represents stretch values of 1.5 or lower.

useful and is defined as follows. The oxidation rates along the edges of the channel (the entrance, the exit and the corners which are defined by the intersection of the channel surface with the channel symmetry plane) are computed and stored for each of the rows and columns of the channel surface mesh. These rates serve to define values for each of the surface mesh points making use of parabolas associated with each of the rows and columns of the surface mesh. Figure 6 shows two examples of parabolic curves for a row and a column at the middle of the surface mesh. For this specific case, there are therefore 57 times 238 parabolic surface curves which are recomputed every time the surface is morphed, or every 1 s.

The surface regression is then performed in two steps. We first morph each surface mesh point by moving it half of the local computed CFD defined oxidation rate from the parabolic expression for the row that it belongs to. We then repeat the procedure again for each surface mesh point but now move it from the parabolic value depending on its associated column. In such a way we take into account the rate along all of the channel corners when computing the amount of necessary displacement for each of the surface mesh points. This gives a more realistic and a more three-dimensional meshing friendly approximation of the surface than a surface advancement based on the actual local CFD oxidation rates for the initial 100 s of modeled surface regression. After the initial 120 s of modeled experimental time, the channel is sufficiently opened for the CFD data to be obtained in a faster manner and we proceed with the oxidation rates obtained based on the CFD solution at each of the surface locations. However, this is not the final mesh which can be directly used in the three-dimensional volume meshing, since it is not integrated with the rest of the surfaces which define the boundaries of the specimen. The resulting mesh is taken back into Gridpro and is used as a control net to produce the spline surface to be integrated with the outer surface of the specimen. Finally the spline-based surface mesh is used in Gridpro to account for the channel surface mesh change, and a new three-dimensional volume computational mesh is created.

C. Computational Fluid Dynamics Technique

The numerical solution of the N–S equations for viscous flow was obtained by use of the Gasp N–S solver [31] using the finite-volume discretization of the computational domain performed with the Gridpro [19] meshing software. Temperature jump and velocity slip corrections to the boundary conditions were used to account for the rarefaction effects inside the channel. To model the channel expansion due to atomic oxygen attack, i.e., Eq. (1), the specific boundary conditions for modeling the chemical processes at the walls of the channel $C_{(s)} + O \rightarrow CO$ were added to Gasp. The numerical boundary condition uses an iterative procedure to solve for the mass fractions at the wall. The implementation details can be found in [32]. Note that the external flow Mach number is sufficiently low that the degree of nitrogen dissociation is small. Therefore, nitridation of the exposed carbon wall was neglected. It was found that the chemical reactions among gas species (such as $O + N_2 \rightarrow NO + N$) are rare in the channel flow since the total reaction energy of the colliding molecules for a gas temperature of 4000 K is usually less than the chemical activation energy. Hence gas-gas chemical reactions were not modeled in either Case 1151 or 2033 discussed below.

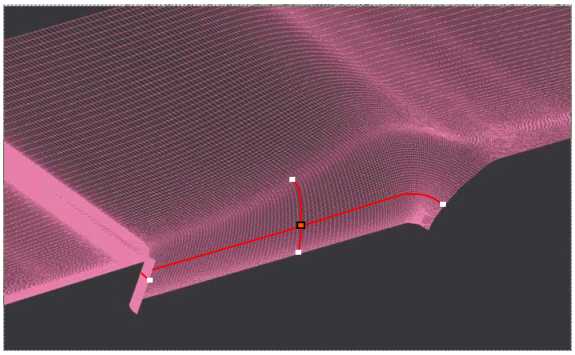

Fig. 6 The analytical approximation of the channel surface.

We also assumed a noncatalytic wall boundary condition. The degree of surface catalycity usually models the fraction of atomic oxygen that recombines at the vehicle wall to form molecular oxygen. This process is important for chemically-nonreacting walls such as silica and the degree of which it is modeled will affect the heat flux to wall. In our damage assessment modeling, however, the affect of the nonexposed (protective coating still intact) is of minor importance because the damage site is sufficiently large. This is why no atomic oxygen recombination to the molecular oxygen was modeled.

The other boundary conditions were as follows. We used the first order extrapolation boundary condition at the exit of the channel in Case 2033 and at the exit of the specimen interior in Case 1151. In earlier work we modeled the interior of the specimens taking into account the holder geometry. In the arcjet test, the inner flow reenters the main flow through large clearances between the holder and the model. The simplification used in this work did not affect the channel flow since the channel is choked. At the specimen walls facing the arcjet flow the velocity no-slip and temperature no-jump conditions were used.

The convergence of the N–S solutions was checked in the following way. Mesh convergence was guaranteed by using three meshes of the same topology but of different density. To facilitate changing the mesh density, a procedure available in Gasp was used, that allows one to coarsen the original computational mesh. The initial solution to a selected number of test cases was obtained on meshes that were coarsen by a factor of four in the X and Y directions. This solutions were later refined with meshes of density reduced by a factor of two compared with the original mesh. Finally the solutions were further refined by interpolating the previously obtained coarser mesh solutions onto the original dense mesh and continuing the solution with the interpolated solution as an initial guess. After a reduction of the residuals by a factor of three orders of magnitude all three of the solutions were compared in the area of interest (the entrance and the interior of the channel). While some difference existed between the two first solutions, the difference in the solutions obtained on the mesh coarsened by a factor of two and the final solution was very small (within less then a percent when the pressure levels were compared). This level of convergence was believed to be acceptable considering of the uncertainties in the problem.

IV. Results and Discussion of Case 1151

A. Case 1151 with Delamination Meshing and Flow Results

An arcjet flow through a hole of a diameter of 0.00325 m and length of 0.006 m was modeled. The solution started from the freestream NATA predicted arcjet conditions presented in Table 1. The layout of the computational domain, presented in Fig. 7, allowed for the adjustment of the zone boundaries to automatically improve the mesh quality in terms of its orthogonality skewness and aspect ratio. To account for the possible influence of delamination, a subchannel was added to the layout of the computational domain as shown in Figs. 7 and 8. Such a microchannel placed at the wall of the main channel can produce a local flow disturbance leading to the intensified oxidation of the wall and weakening of the material structural integrity. After a preliminary CFD solution, based on a coarser mesh, the position of the shock wave was determined and the mesh was adapted to better capture the shock wave gradients, as presented in Fig. 9. To better resolve the boundary layer gradients mesh points were clustered at the walls as presented in Fig. 10. It can be seen that the mesh cells are orthogonal with small aspect ratio (excluding the cells in the boundary layer) and with almost no skewness in 80 to 90% of the cells.

To resolve mesh singularities at the corners of the specimen and at the entrance of the subchannel, artificial double-sided surfaces were introduced into the computational model at the mesh generation stage. After each of the sequential computations, the channel walls and adjacent boundaries (including artificial walls) were morphed

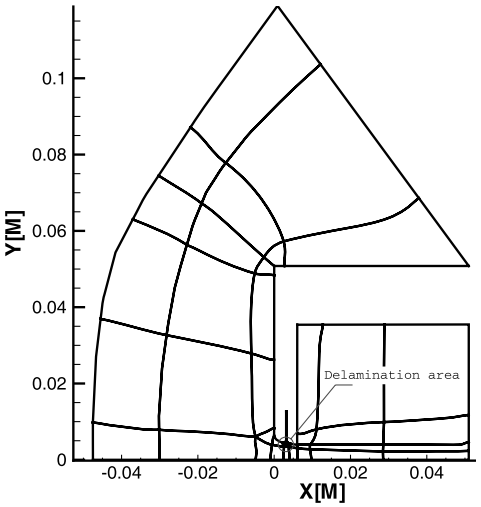

Fig. 7 Multizone layout of the computational domain. The presented case corresponds to 50 s.

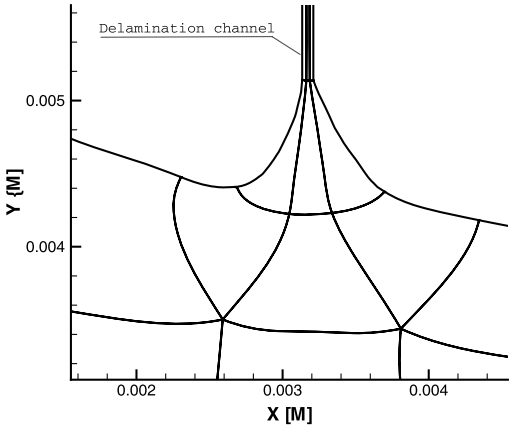

Fig. 8 The domain layout in vicinity of the subchannel. Mesh-block structure reflects the user provided topology. The resulting mesh structure allows for a proper resolution of the flow gradients in the multiscale Case 1151 with delamination.

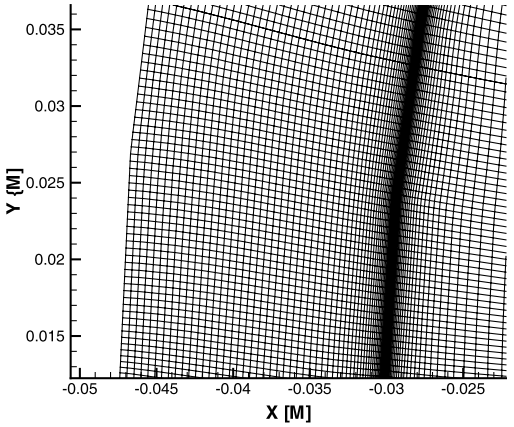

Fig. 9 Mesh adaptation in the shock wave area allowed for a better gradient resolution.

and the new computational domain was remeshed in a semi-automated manner. Mesh quality was checked for skewness with tools available in Gridpro for each of the solved cases. The worse values of the parameters measuring the mesh quality were as follows, skewness: 0.4452, aspect stretching ratio: 3.858, smoothness (turn

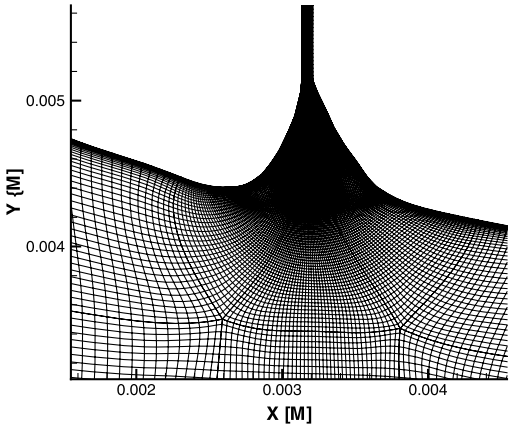

Fig. 10 The subchannel entrance meshing. Mesh clustering close to the wall is presented along with the overall quality of the mesh in vicinity of the subchannel entrance.

angle) 83.612, aspect ratio 148.2. It should be noted that the large aspect ration is not a concern in the clustered meshes resolving the boundary and shock wave gradients. The mesh gradients are extremely large in the cases with a subchannel since the outer flow, channel flow, and the subchannel flow were all solved in a single run starting from the preshock NATA solution. However, the mesh quality was never allowed to worsen below the strict limits imposed by the checking procedures. After morphing the surface, the remeshing of the computational domain was relatively straightforward with a limited amount of manual work.

B. Influence of Delamination

To understand the behavior of the flow parameters influencing the main channel wall regression rate, temperature and atomic oxygen mass fraction are presented in Figs. 11a and 11b. Additionally CO mass fraction and velocity streamlines are presented in Figs. 11c and 11d. Figure 12 presents a comparison between the oxidation rates at the channel wall for 0 and 50 s. Finally Fig. 13 presents a comparison between the computational results for calculations with and without the subchannel or delamination with the experimental data. Figure 11 shows that for the expanded subchannel the flow in the subchannel entrance area stagnates with recirculation areas observed. This results in the atomic oxygen available in the subchannel area being consumed by the chemically active wall, and CO, the product of the oxidation, remains in the subchannel entrance area shielding the fresh intake of additional atomic oxygen from the channel flow. This in turn results in a lower oxidation rate in the subchannel area compared with that along the main channel wall as can be seen in Fig. 12. Figure 12 demonstrates that this occurs because the 50 s surface regression profile is actually reversed compared with the initial (0 s) result. The phenomena is probably due to two different factors contributing to the oxidation rate: pressure build up at the subchannel corners and the stagnation of the flow in the subchannel area. These factors influence the oxidation rate magnitude in different directions. A more accurate direct simulation Monte Carlo method or Bhatnagar, Gross and Krook model solution to the subchannel inlet problem may provide more insight into the phenomena since the local Knudsen which is on the order of 0.1 suggests that the flow regime is transitional and the kinetic approaches may be useful.

The entrance and exit hole diameters growth, presented in Fig. 13, show the influence of the delamination (the presence of the subchannel) on the main channel regression. As can be seen in the figure, the presence of the subchannel increases the rate of the exit diameter growth compared with the results of the computation without the subchannel. This influence brings the computational results closer to the experimental data. At the same time, the growth of the entrance diameter of the channel remains the same and does not depend on the presence of the subchannel. The modeling of nonequilibrium shock layer chemistry also introduces uncertainties into the material response. In [33] a sensitivity study was performed to determine the

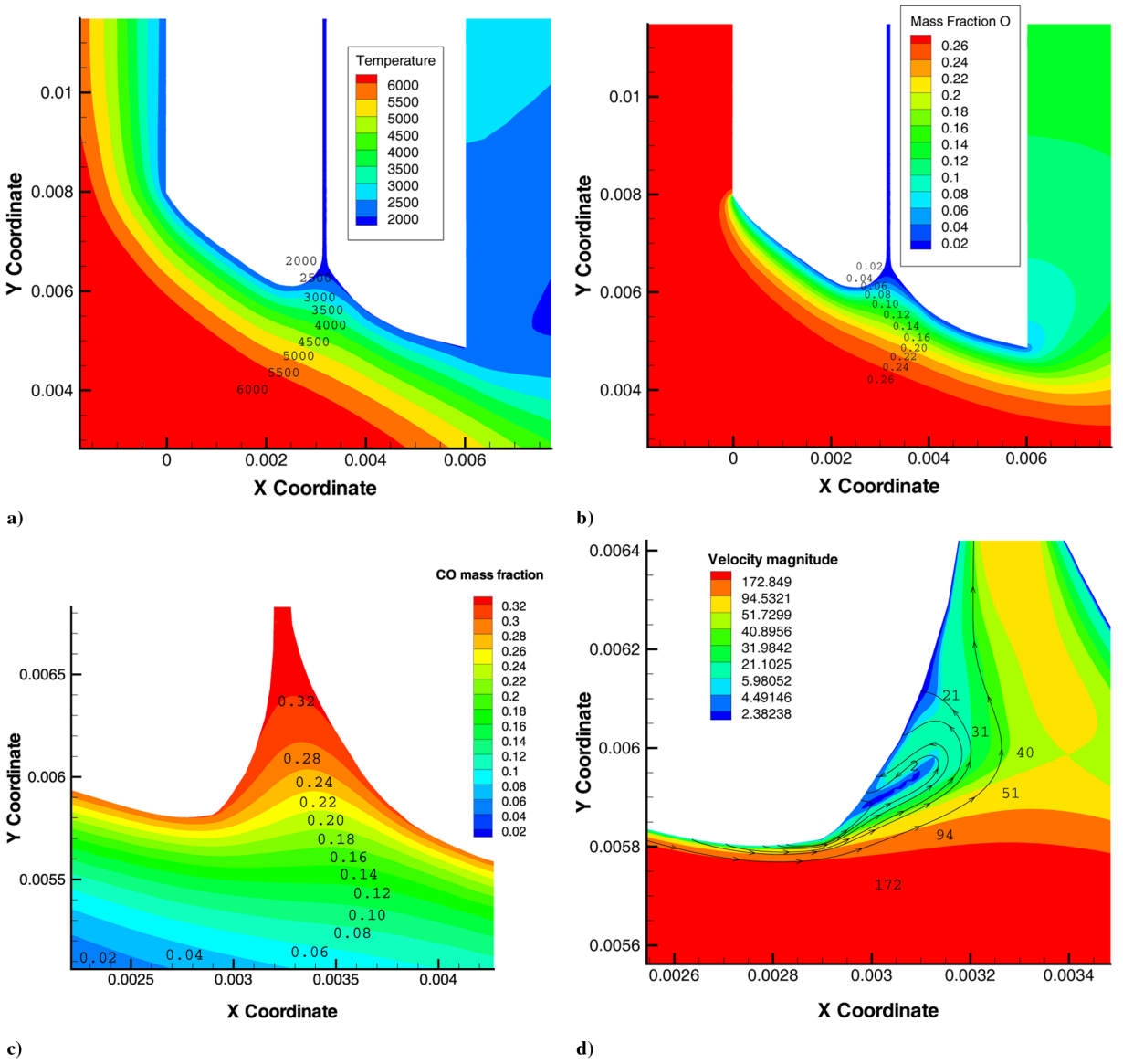

Fig. 11 Flow parameters: a) temperature, K, b) oxygen mass fraction, c) CO mass fraction, and d) velocity magnitude, m/s, contours in the channel and the streamlines.

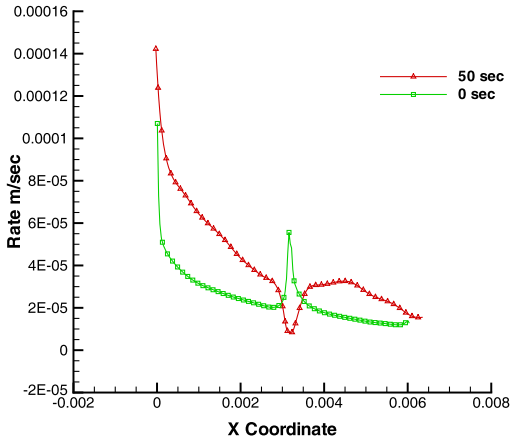

Fig. 12 Oxidation rates at 0 and 50 s, m/s.

affect of additional atomic oxygen on the hole rate growth. If the mass fraction of atomic oxygen in the shock layer increases from approximately 0.2 to 0.27 it was found that the additional atomic oxygen noticeably affects the channel entrance region oxidation rate, but has little impact on the outlet diameter, unlike the inclusion of the subchannel.

V. Results and Discussion of Case 2033

The top portion of Fig. 14 provides a schematic of the three-dimensional wedge case geometry and the layout of the computational domain associated with it. The CFD solution started from the freestream arcjet conditions presented in Table 1. Presented in the figure is the 320 s case, with the channel already substantially expanded to demonstrate all of the features of the computational domain. The initial channel dimensions were 0.990×38.1 mm (0.0387×1.5 in.) with a depth of 6 mm. The multiscale external–internal flow for this setup was solved in a single run. The computational domain was structurally meshed using the techniques described in Sec. III The computational domain consisted of the larger outer subdomain and a tiny well meshed microchannel domain. Top portion of the Fig. 14 also presents the mesh-block structure which was optimized to produce a high-quality three-dimensional mesh covering the entire computational domain. The inlet surface presented in the figure was set up with the boundary conditions corresponding to the freestream NATA preshock solution as for the Case 1151 (see Table 1). No-slip thermal boundary conditions were set at the surface of the specimen, which is marked as

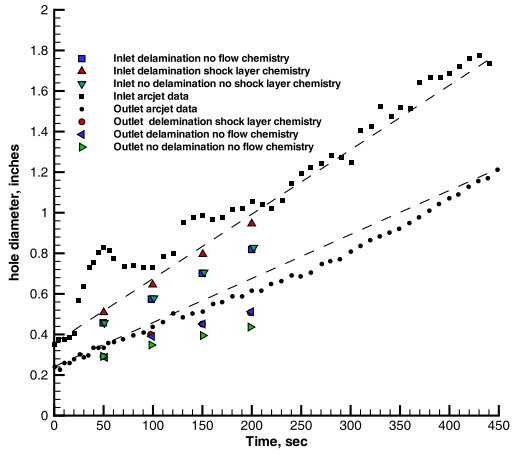

Fig. 13 Wall regression. Entrance and exit hole diameters. N–S results with and without subchannel and additional atomic oxygen, m/s. Data taken from [1].

wedge in the figure, while temperature jump velocity slip boundary conditions with oxidation at the wall were used at the channel walls. First order extrapolation boundary conditions were set at the two exits of the computational domain, and two symmetry planes were used to limit the computational domain in the Z direction. The flow direction is also presented in the figure as a vector in the XY plane, making 45 deg angle with the X axis. The bottom portion of Fig. 14 presents the computational mesh. The total number of blocks and mesh points used was approximately 50 and 1.4 million, respectively. Figure 15 further illustrates the features of the computational domain by presenting the Mach number contours obtained from a CFD solution with use of the presented computational mesh. In particular the supersonic free stream, the shock layer and the low Mach number flow inside the channel can be observed.

To model the 2033 case flow, the mesh-block structure in the shock region and the channel are crucial. To better illustrate the channel portion of the computational domain, a mesh block which corresponds to the channel and its entrance area is presented in Fig. 16. As can be seen in the figure, nine mesh blocks each with a typical cell size of 0.00012 m were used to mesh the channel area to obtain adequate resolution of the boundary layer, since the flow properties at the walls of the channel are essential for the correct prediction of the channel expansion. Figure 17 presents the atomic oxygen density contours plotted in three dimensions using the excerpt of the computational mesh, presented in Fig. 16. To illustrate the capturing of the three-dimensional shock wave, a portion of the computational domain with the exposed interior of the mesh is presented in Fig. 18. This is a 60 s case mesh which was used in the series of solutions covering the expansion of the channel. As can be seen in the figure to capture the shock, the mesh resolution is significantly higher in the shock wave area, with a typical mesh cell size of 5.0×10^{-5} m.

A series of N–S calculations was performed based on computational domains similar to the one presented in Fig. 14 at 0,

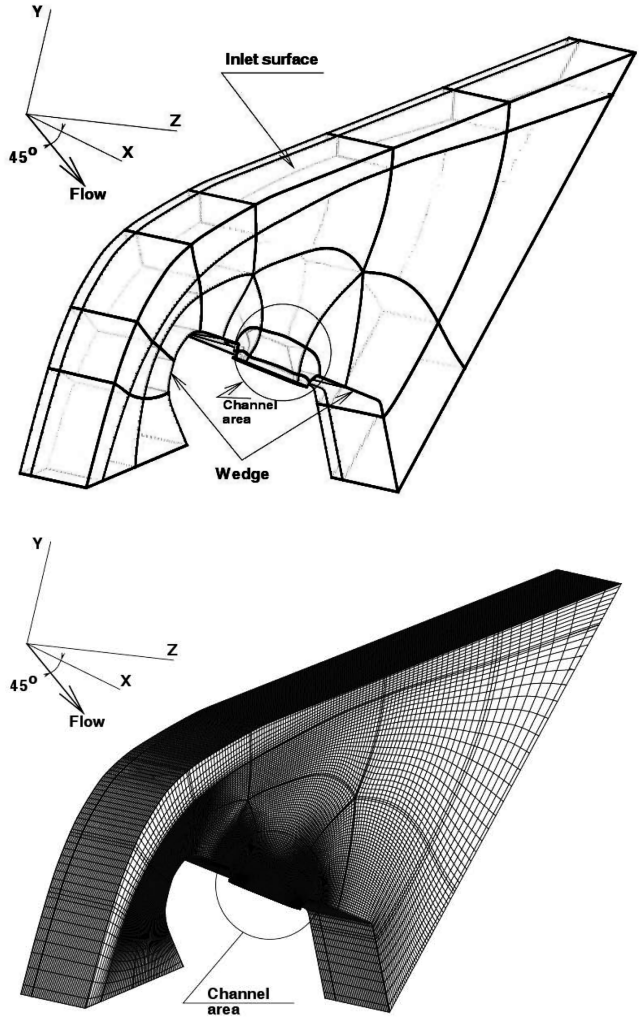

Fig. 14 320 s case. Topology of the computational domain (top) and the computational mesh (bottom).

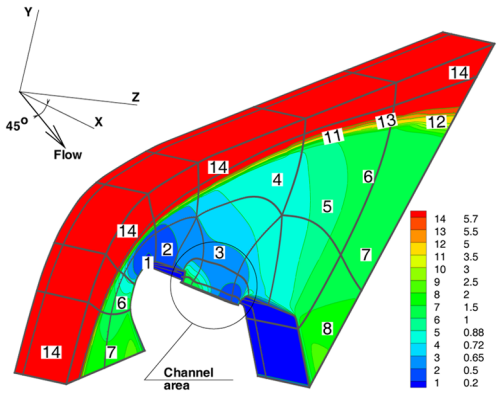

Fig. 15 320 s case Mach number contours in the three-dimensional computational domain.

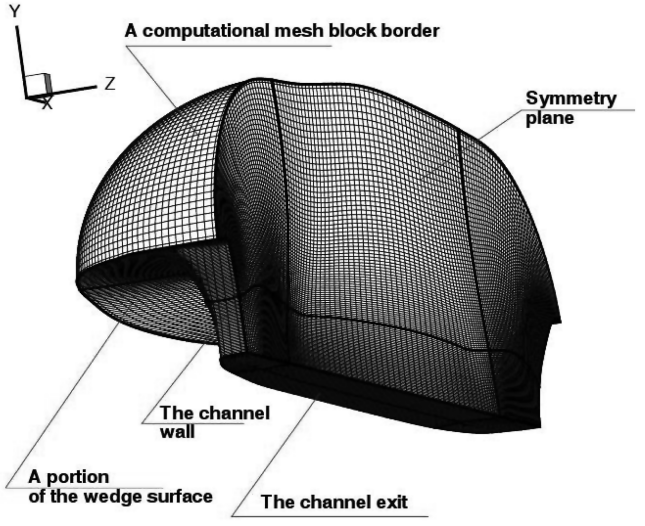

Fig. 16 320 s case. An excerpt of the computational mesh in vicinity of the channel area.

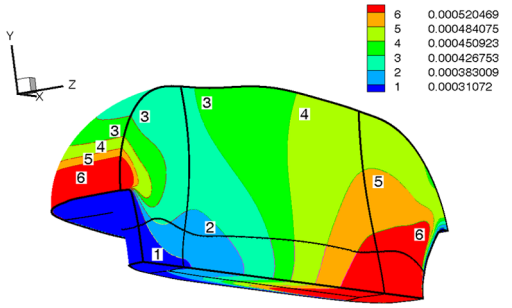

Fig. 17 320 s case. Atomic oxygen number density in vicinity of the channel.

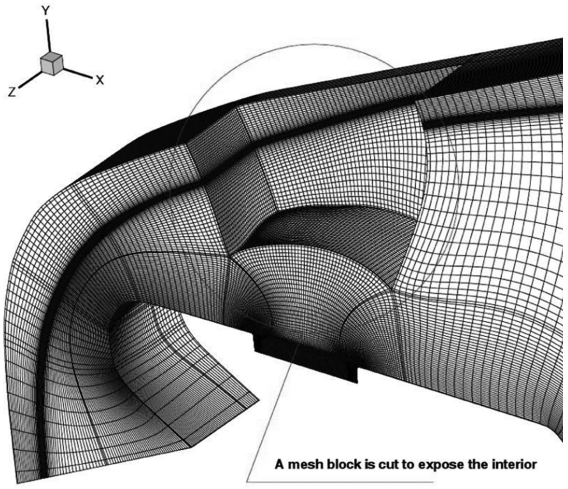

Fig. 18 60 s case. Computational mesh. Illustration of the shock wave capturing.

60, 120, 220, 320 and 420 s. Figure 19 shows the major flow features in the computational domain, namely Mach number, pressure and temperature contours for one of these iterations at 60 s. As can be seen in the figures the overall flow features are well resolved and show the expected spatial distributions in all portions of the computational domain. In particular, the shock wave structure is resolved and the flow inside the channel is accurately modeled. Figure 20 shows the atomic oxygen and CO mass fraction distribution at the channel walls and over the specimen for the 60 s case. As can be seen in the figure, a small portion of the reaction product of at the walls of the channel escapes the channel through the subsonic boundary layer and moves over the specimen. A corresponding decrease in the atomic oxygen mass fraction can also be observed in Fig. 20. Such a mechanism actually reduces the specimen surface destruction in the downstream area since the product of reaction, the CO generated inside the channel, when escaping the channel, shields the specimen surfaces from the chemically active atomic oxygen.

The top portion of Fig. 21 presents the shape of the channel computed at different times. During the first two computational steps, 0 and 60 s, the parabolic surface approximation defined in Sec. III was used. After the channel was sufficiently opened with its walls exposed to the coming flow, beginning with 120 case, the local surface displacements were computed based on the direct use of local oxidation rates obtained from the CFD solutions. The local oxidation rates could be used directly before 120 s, however, the degree of coupling between the CFD and surface morphing required would be prohibitively high. The rest of the procedure as described in Sec. III remained the same.

The following observations can be made from the results of modeling. The initial channel expansion is less intensive and more

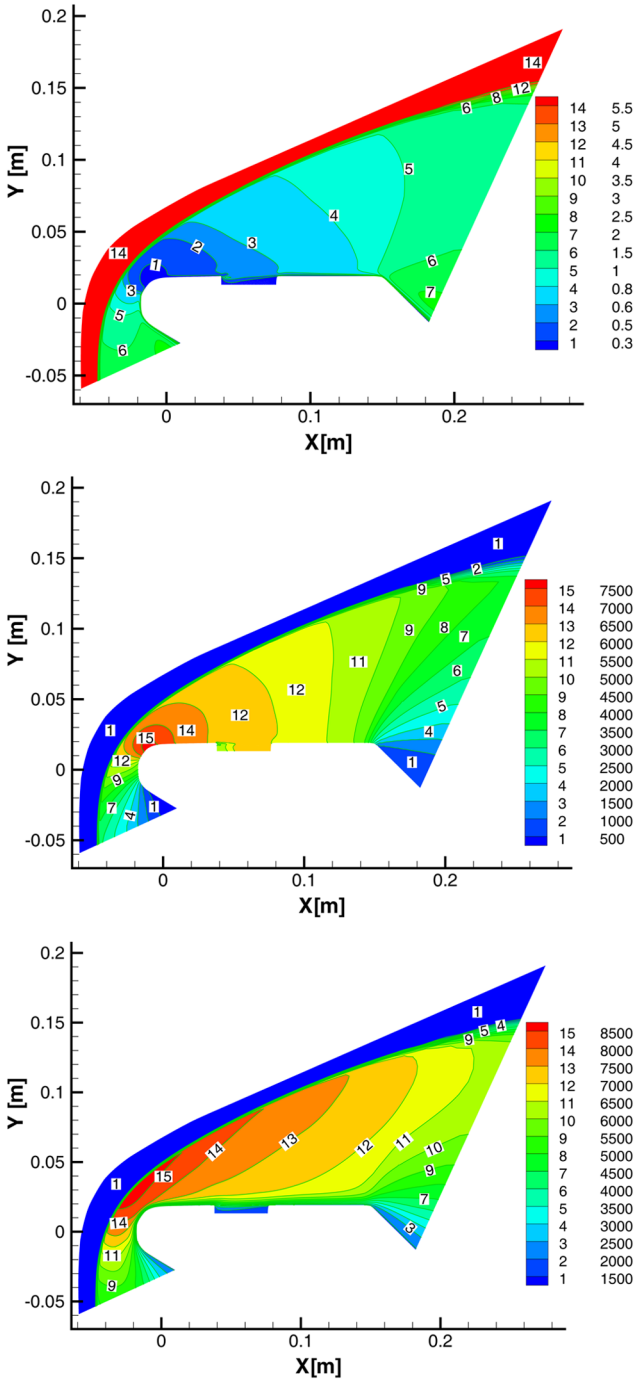

Fig. 19 60 s case. Mach number, pressure, temperature contours in the symmetry plane.

even in all of the directions. However, when the channel opens, which allows more atomic oxygen to enter the channel interior, the process accelerates, with the predominant expansion areas being formed in the downstream portion of the channel.

The bottom portion of Fig. 21 shows a comparison between the channel shapes obtained computationally and experimentally in the arcjet facility. The experimentally obtained surface was reconstructed based on the posttest measurements of the channel. As can be seen in the figure the channel sizes are in a good agreement at the entrance of the channel with the experimentally obtained channel being slightly larger. The size of the experimental channel at the exit is approximately 20% smaller than that of the computational one. The overall shapes of the channels are remarkably close.

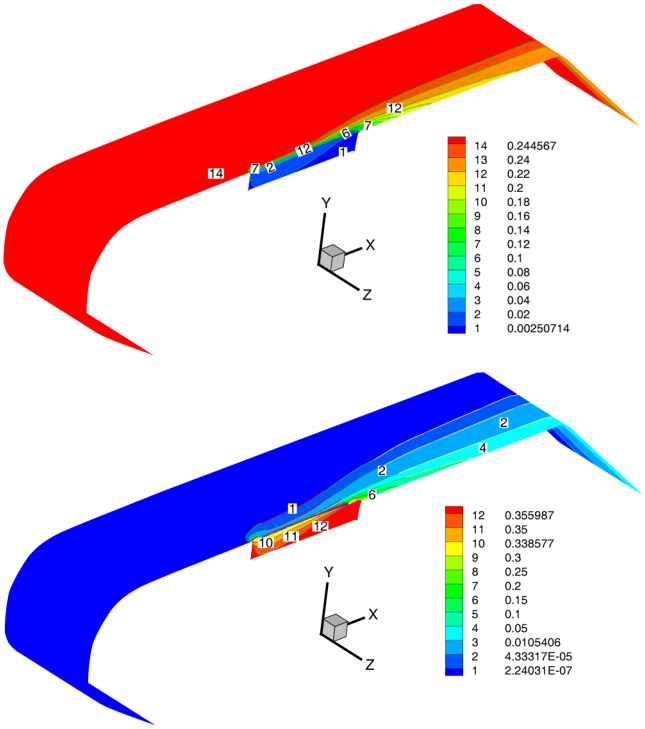

Fig. 20 60 s case. O (top) and CO (bottom) mass fraction over the specimen.

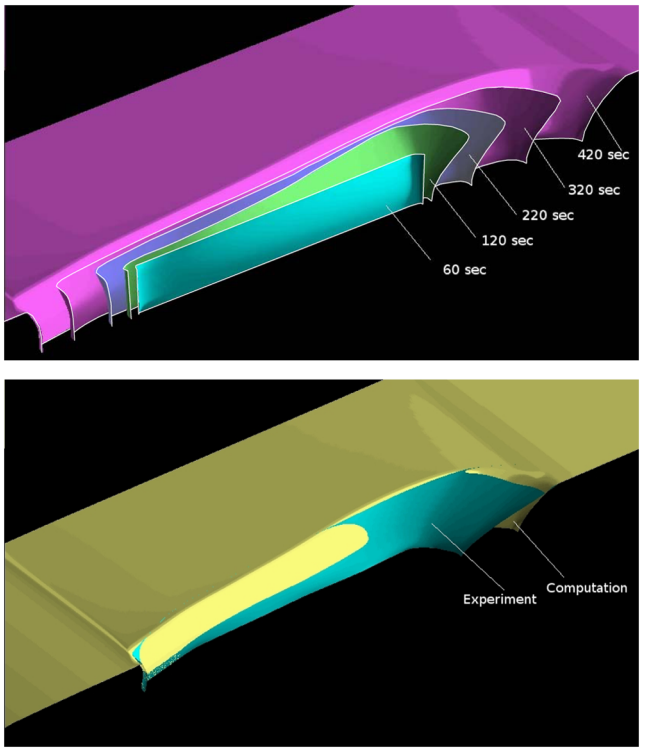

Fig. 21 Channel shape at different times (top) and comparison of the computationally obtained and the posttest shapes of the channel (bottom).

VI. Conclusions

In this work, an approach was developed to model the continuum flow through the carbon-crack channel of RCC test samples. The gas dynamics was modeled using the N–S technique with chemically active boundary conditions. Atomic oxygen impacting a bare carbon wall was assumed to chemically react with the wall to produce CO gas (with a probability of 0.9) that enters the flowfield. The first configuration considered, referred to as Case 1151, was a stagnation area hole flow simulation, similar to that which can occur in the space shuttle nose cap. The case was modeled with and without delamination and the shock layer chemistry with the results compared with the experimentally obtained data on the channel-hole growth. The second specimen, referred to as Case 2033, was a model of the space shuttle leading edge with a narrow microchannel cut through its surface. For this case, advanced approaches to meshing the recessing channel walls iterated with computationally intensive three-dimensional CFD N–S solutions which produced a channel shape and size similar to that observed experimentally after 420 s of the specimen exposure to the high-energy arcjet flow.

The computational results confirm the hypothesis that the carbon surface degradation is mainly caused by flow atomic oxygen reacting with the carbon wall material. The results show no significant impact of the delamination on the hole inlet diameter growth, however, the exit diameter of the hole is impacted by the microstagnation area which is formed at the entrance of the subchannel causing delamination. It was also found that the shock layer production of the additional atomic oxygen can impact the channel wall recession rate since the rate is proportional to the amount of the atomic oxygen available for the gas-surface reaction.

The developed three-dimensional surface morphing procedure used to account for the channel shape change for the model 2033, when coupled with the topology-based meshing approach, provided a robust tool for modeling the specimen surface recession due to the chemistry at the wall. The developed procedure and the software code is planned to be used to model the space shuttle microchannel growth under the operational conditions as the created mesh topology can be used for similar cases of cracked TPS modeling. Applications to the NASA new generation Crew Exploration Vehicle/Orion spacecraft are also being developed.

Acknowledgments

E. V. Titov and D. A. Levin would like to acknowledge support from Boeing Contract No. 6H08845 and NASA Grant NNX08AD84G from NASA Johnson Space Center. We would especially like to thank the AeroSoft Corporation, Blacksburg, VA, for their technical support and assistance in incorporating the gas wall oxidation boundary condition.

References

[1] Curry, D. M., Pham, V. T., Norman, I., and Chao, D. C., "Oxidation of Hypervelocity Impacted Reinforced Carbon–Carbon," *Journal of Spacecraft and Rockets*, Vol. 37, No. 3, 2000, pp. 310–317. doi:10.2514/2.3580

[2] Titov, E., Zhong, J., Levin, D., and Picetti, D., "Simulation of Carbon–Carbon Crack Growth due to Carbon Oxidation in High Temperatures," *Journal of Thermophysics and Heat Transfer*, Vol. 23, No. 3, July–Sept. 2009, pp. 489–501.

[3] Curry, D., Pham, V., Norman, I., and Chao, D., "Oxidation of the Reinforced Carbon–Carbon Subjected to Hypervelocity Impact," NASA TP 2000-209760, March 2000.

[4] Moss, J., Glass, C., and Greene, F., "DSMC Simulations of Apollo Capsule Aerodynamics for Hypersonic Rarefied Conditions," 9th AIAA/ASME Joint Thermophysics and Heat Transfer Conference, AIAA Paper No. 2006-3577, 2006.

[5] Scala, S., and Gilbert, L., "Sublimation of Graphite at Hypersonic Speeds," *AIAA Journal*, Vol. 3, No. 9, Sept. 1965, pp. 1635–1644. doi:10.2514/3.3220

[6] Bacos, M. P., Dorvaux, J. M., Lavigne, O., and Renollet, Y., "C/C Composite Oxidation Model 1. Morphological Experimental Investigations," *Carbon*, Vol. 38, No. 1, 2000, pp. 77–92. doi:10.1016/S0008-6223(99)00103-7

[7] Bacos, M. P., Cochon, J. L., Dorvaux, J. M., and Lavigne, O., "C/C Composite Oxidation Model 2. Oxidation Experimental Investigations," *Carbon*, Vol. 38, No. 1, 2000, pp. 93–103. doi:10.1016/S0008-6223(99)00104-9

[8] Bacos, M. P., Dorvaux, J. M., Lavigne, O., and Talandier', J., "C/C Composite Oxidation Model 3. Physical Basis, Limitations, And Applications," *Carbon*, Vol. 38, No. 1, 2000, pp. 105–117.

doi:10.1016/S0008-6223(99)00105-0

[9] Jacobson, N., Leonhardt, T., Curry, D., and Rapp, R., "Oxidative Attack of Carbon/Carbon Substrates Through Coating Pinholes," *Carbon*, Vol. 37, No. 3, 1999, pp. 411–419. doi:10.1016/S0008-6223(98)00206-1

[10] Hatta, H., Aoki, T., Kogo, Y., and Yarii, T., "High-Temperature Oxidation Behavior of SiC-Coated Carbon Fiber-Reinforced Carbon Matrix Composites," *Composites Part A*, Vol. 30, May–June 1999, pp. 515–520. doi:10.1016/S1359-835X(98)00143-2

[11] Curry, D., Johansen, K., and Stephens, E., "Reinforced Carbon–Carbon Oxidation Behavior in Convective and Radiative Environments," NASA TP 1284, 1978.

[12] Rosner, D., and Allendorf, H., "Kinetics of the Attack of Refractory Materials by Dissociated Gases," *Proceedings of an International Conference in Metallurgy and Materials Science Held at the University of Pennsylvania*, May–June 1970, pp. 231–251.

[13] Rosner, D., and Allendorf, H., "High-Temperature Kinetics of Graphite Oxidation by Dissociated Oxygen," *AIAA Journal*, Vol. 3, No. 8, Aug. 1965, pp. 1522–1523. doi:10.2514/3.3186

[14] Williams, S., Curry, D., Chao, D., and Pham, V., "Ablation Analysis of Shuttle Orbiter Oxidation Protected Reinforced Carbon–Carbon," *Journal of Thermophysics and Heat Transfer*, Vol. 9, No. 3, July–Sept. 1995, pp. 478–485.

[15] Sokolinsky, V., Housner, J., Surdenas, J., and Abdi, F., "Progressive Failure Analysis of Shuttle Reinforced Carbon–Carbon Plate Specimens," 47th AIAA/ASME/ASCE/AHS/ASC Structures, Structural Dynamics and Materials Conference, AIAA Paper No. 2006-1781, May 2006.

[16] Heinrich, R., *Implementation and Usage of Structured Algorithms Within an Unstructured CFD-Code, Notes on Numerical Fluid Mechanics and Multidisciplinary Design*, Springer–Verlag, Berlin, 2007.

[17] Beall, M., and Shephard, M., "A General Topology-Based Mesh Data Structure," *International Journal for Numerical Methods in Engineering*, Vol. 40, No. 9, 1997, pp. 1573–1596. doi:10.1002/(SICI)1097-0207(19970515)40:9<1573::AID-NME128>3.0.CO;2-9

[18] Anderson, D., "Adaptive Grid Methods for Partial Differential Equations," ASME/FED Conference, May 1983.

[19] Eiseman, P. R., "Adaptive Grid Generation," *Computer Methods in Applied Mechanics and Engineering*, March 1987, pp. 321–376. doi:10.1016/0045-7825(87)90046-6

[20] Akleman, E., and Chen, J., "Guaranteeing 2-Manifold Property for Meshes by Using Doubly Linked Face List," *International Journal of Shape Modeling*, Vol. 5, No. 2, 2000, pp. 149–177.

[21] Akleman, E., Chen, J., Srinivasan, V., and Eryoldas, F., "A New Corner Cutting Scheme with Tension and Handle-Face Reconstruction," *International Journal of Shape Modeling*, Vol. 7, No. 2, 2001, pp. 111–121. doi:10.1142/S0218654301000084

[22] Akleman, E., Chen, J., and Srinivasan, V., "A Minimal and Complete Set of Operators for the Development of Robust Manifold Mesh Modelers," *Graphical Models*, Vol. 65, No. 5, 2003, pp. 286–304. doi:10.1016/S1524-0703(03)00047-X

[23] Delzanno, G., Chacon, L., Finn, J., Chung, Y., and Lapenta, G., "An Optimal Robust Equidistribution Method for Two-Dimensional Grid Adaptation Based On Monge–Kantorovich Optimization," *Journal of Computational Physics*, Vol. 227, No. 23, 2008, pp. 9841–9864. doi:10.1016/j.jcp.2008.07.020

[24] Dwyer, H., and Onyrjrkwe, O., "Generation of Fully Adaptive and/or Orthogonal Grids," *Proceedings of the Ninth International Conference on Numerical Methods in Fluid Dynamics*, Saclay, France, 1984.

[25] Jeng, Y., and Lee, Z., "Revisit to the Modified Multiple One-Dimensional Adaptive Grid Method," *Numerical Heat Transfer Part B*, Vol. 29, 1996.

[26] Bracbill, J., and Saltzman, J., "Adaptive Zoning for Singular Problems in Two Dimensions," *Journal of Computational Physics*, 1982.

[27] Azarenok, B., "Variational Method for Adaptive Mesh Generation," *Computational Mathematics and Mathematical Physics*, Vol. 48, No. 5, 2008, pp. 786–804. doi:10.1134/S0965542508050084

[28] Titov, E., Kumar, R., Levin, D., Larin, M., and Anderson, B. P., "Modeling of Crew Exploration Vehicle Re-Entry Ablation Flows," AIAA Paper No. 2010-0988, 2010.

[29] Lewis, R., "Quick Look Report," *Atmospheric Reentry Materials and Structures*, Jan. 2004.

[30] Alter, S. J., "A Structured-Grid Quality Measure for Simulated Hypersonic Flows," AIAA Paper No. 2004-612, Jan. 2004.

[31] GASP, General Aerodynamic Simulation Program, Computational Flow Analysis Software for the Scientist and Engineer, User's Manual, Aerosoft Co., Blacksburg, VA, 1996.

[32] Milos, F., "Review of Numerical Procedures for Computational Surface Thermochemistry," *Journal of Thermophysics and Heat Transfer*, Vol. 8, No. 1, 1994.

[33] Titov, E., Levin, D., Picetti, D., and Anderson, B., "Simulation of TPS Crack Growth due to Carbon Oxidation Using Advanced Grid Morphing Techniques," 41st AIAA Thermophysics Conference, AIAA Paper No. 2009-3599, 22–25 June 2009.